Chapter-3

Nanocrystalline β-NiS: A Redox-Mediated Electrode in Aqueous Electrolyte for Pseudocapacitor/Supercapacitor Applications

Chapter-3

Nanocrystalline β-NiS: A Redox-Mediated Electrode in Aqueous Electrolyte for Pseudocapacitor/Supercapacitor Applications

3.1 Introduction

The utilization of NiS as a supercapacitor electrode was first reported by Hou et al. [1] in which an electrochemical reaction mechanism was proposed. Zhu et al. [2] designed and fabricated hierarchical hollow structures to examine the increased electrochemical performance of nickel sulfide. In the recent years, NiS has drawn much attention because of its exceptional electrical conductivity, low toxicity, affordability, simplicity of manufacture, and plethora of valance states. [3-8] NiS are frequently used as catalysts for hydrogenation and carbon liquefaction events and to store solar energy. [9] Additionally, their impact on toughened glass and their carcinogenic consequences have drawn much investigation.

NiS, NiS_2, Ni_3S_2, Ni_3S_4, and Ni_9S_8, as well as amorphous and nanocrystalline phases, are among the known solid phases of nickel sulfides. The most prevalent nickel sulfide minerals among these solid phases are millerite (NiS), heazlewoodite (Ni_3S_2), polydymite (Ni_3S_4), and vaesite (NiS_2). There are two types of nickel(II) monosulfide (NiS, namely NiAs-type NiS (also known as α-NiS; space group $P6_3/mmc$) [10] and millerite (also known as β-NiS; space group R3m). At low temperatures (below 652 K), millerite is the stable form of NiS, but at higher temperatures, NiAs-type NiS is more stable. The most prevalent nickel sulfide mineral and nickel ore mineral is millerite. [11]

In this chapter, we present the synthesis procedure, characterizations, and electrochemical performances of β-NiS nanoparticles. Nanoparticles of nickel sulphide shows the phonon confinement effect as confirmed by its Raman and UV-visible spectra. The β-NiS electrode has a specific capacitance of 1578 F/g at 1 A/g from the galvanostatic discharge profile, whereas a capacitance of 1611 F/g at 1 mV/s was obtained through CV curve in 2 M KOH aqueous electrolyte. Additionally, we have assembled aqueous asymmetric supercapacitors (ASCs) with activated carbon (AC) as the negative electrode and the β-NiS electrode as the positive electrode. These combinations of β-NiS electrode with AC gave excellent cyclic stability, which resulted in the highest specific energy, equivalent to ~163 Wh/kg and a specific power of ~507 W/kg, which are reported in the subsequent sections.

3.2 Experimental:

3.2.1 Synthesis Method

For the synthesis of β-NiS, 5.94 g (0.1 M) of nickel (II) chloride hexahydrate ($NiCl_2.6H_2O$) was dissolved in 250 ml of deionized water with continuous stirring for 4-5 hrs to make a homogeneous solution, followed by the passing H_2S gas (synthesized by the Kipp generator method) into the solution. A black precipitate of β-NiS was obtained after a while, which was then filtered and washed several times with deionized water. The products were dried in a hot air oven at 120 °C for 12 h under N_2 atmosphere. The final product was further characterized and tested for its electrochemical performance. The synthesis reaction is given in equation 3.1.

$$NiCl_2.6H_2O + H_2S \rightarrow NiS + 2HCl + 6H_2O \qquad (3.1)$$

3.3 Results and Discussions:

3.3.1 XRD Studies

The XRD pattern of the as-prepared powder sample confirms the purity and formation of the β-phase of NiS nanoparticles. Fig. 3.1a shows the Rietveld refined XRD profile of β-NiS nanoparticles; refinement was done using the program FullProf Suite. Parameters were refined in the space group -R3m and converged to a final R_{bragg} = 4.22 %, R_f = 3.25 %, R_p = 21.4 %, R_{wp} = 14.8 and a goodness of fit (χ^2) of 1.53. The sharp prominent diffraction peaks at 18.46, 30.52, 32.25, 35.9, and 40.66 values of 2θ represent the (110), (101), (300), (021) and (211) planes of β-NiS nanoparticles in the rhombohedral cell (space group: R3m) with lattice parameters a = 9.61(3) Å, b = 9.61(3) Å, c = 3.13(7) Å, α = β = γ = 90°, these data matches very well with the diffraction peaks obtained for β-NiS nanoparticles of ICDD File No: 00-003-0760.

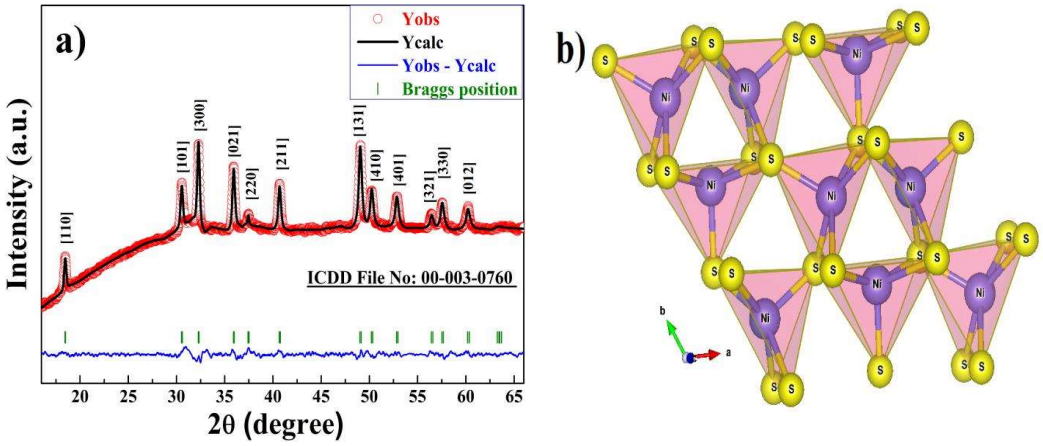

Fig. 3.1 (a) Rietveld refinement of the XRD profile of β-NiS nanoparticles and **(b)** VESTA image of β-NiS nanoparticles.

Table 3.1 shows the crystallographic diffraction data of β-NiS nanoparticles, and crystallite size was calculated using the Debye-Scherrer equation, and the average crystallite size was found to be ~12.6 (±1) nm. The VESTA image Fig. 3.1b shows that β-NiS nanoparticles adopt a rhombohedral millerite phase.

Table 3.1. X-ray crystallographic representative diffraction data for β-NiS nanoparticles

Position(2θ)	**d-spacing (Å)**	**hkl** (Plane)	**Crystallite Size** (nm)
18.457	4.80	1 1 0	33.19
30.521	2.93	1 0 1	18.68
32.255	2.77	3 0 0	17.45
35.904	2.45	0 2 1	15.23
37.416	2.40	2 2 0	14.43
40.662	2.22	2 1 1	12.90
49.028	1.86	1 3 1	9.88
50.213	1.82	4 1 0	9.53
52.825	1.73	4 0 1	9.06
56.440	1.63	3 2 1	7.94
57.516	1.60	3 3 0	7.70
60.185	1.54	0 1 2	7.14
63.260	1.47	0 5 1	6.56
63.528	1.46	2 0 2	6.51
Average Crystallite Size (nm)			**12.59**

3.3.2 Thermal Analysis

Thermogravimetric analysis (TGA) under the N_2 atmosphere was used to understand the thermal stability of β-NiS nanoparticles, Fig. 3.2 a. The as-precipitated black powder was utilized for TGA study. The first two decomposition stage is located between 30 and 220 °C (weight loss of about 6.64%, equivalent to ~0.3 H_2O molecule), which is due to the removal of residual moisture and the hydroxide group. The third stage of weight loss, about 9.12% (equivalent to ~0.4 sulfur loss), occurs in the temperature range of 220–550°C and is attributed to the structural collapse and gradual decomposition of the sample and release of sulfur. [12]

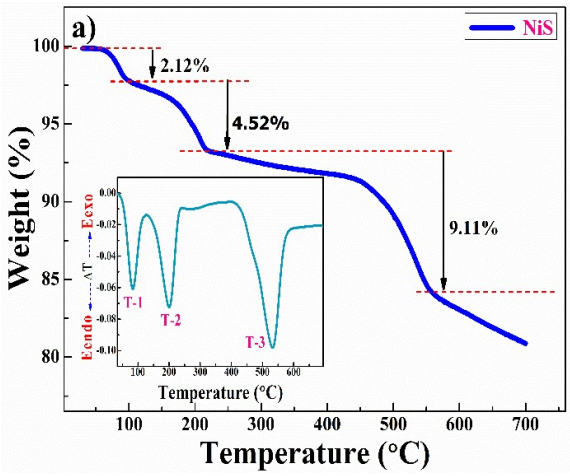

Fig. 3.2 (a) TGA of β-NiS nanoparticles in an N_2 atmosphere (inset shows the DTA plot)

DTA (differential thermogravimetric analysis) shown in the inset clearly shows two endothermic peaks at 83°C and 200°C which is attributed to desorption of the absorbed water and removal of the structural water molecule, while the endothermic peak at 530°C may be attributed to structural collapse and the gradual loss of sulfur resulting in a weight loss of 9.12%. Hence the samples were dried at 120 °C in N_2 atmosphere to make it moisture free. The weight losses that appeared in the TGA study are represented by equations 3.2 & 3.3.

$$NiS.xH_2O \rightarrow NiS + xH_2O \quad ; x \sim 0.3 \qquad (T \sim 220\ ^oC) \qquad (3.2)$$

$$NiS \rightarrow NiS_y + (1\text{-}y)S \quad ; y \sim 0.6 \qquad (T \sim 550\ ^oC) \qquad (3.3)$$

3.3.3 Structural Analysis

Fig. 3.2b presents the FT-IR spectrum of the as-prepared β-NiS nanoparticles. The broad bands at 3297 and 1615 cm^{-1} is attributed to the stretching and bending vibrations, correspondingly of OH groups of water adsorbed to the surface, respectively. [13] The bands at 442, 420, 666, 766 1096 and 984 cm^{-1} are due to the symmetrical and asymmetrical stretch of the Ni-S band in NiS particles, which is in fair agreement to results published. [14]

Raman lines (Fig. 3.2c) for β-NiS nanoparticles (<10 nm) are asymmetrically widened and shifted toward lower wavenumbers due to the quantum confinement of optical phonons related to the particle size of the materials, i.e., red-shifted, indicating the phonon confinement effect. β-NiS nanoparticles show a stretching vibration band around 471 cm^{-1} due to the presence of NiS nanocrystals and high intensity stretching band at 1087 cm^{-1} confirms the phonon confinement effect [11] due to the nano size of β-NiS particles. [15, 16]

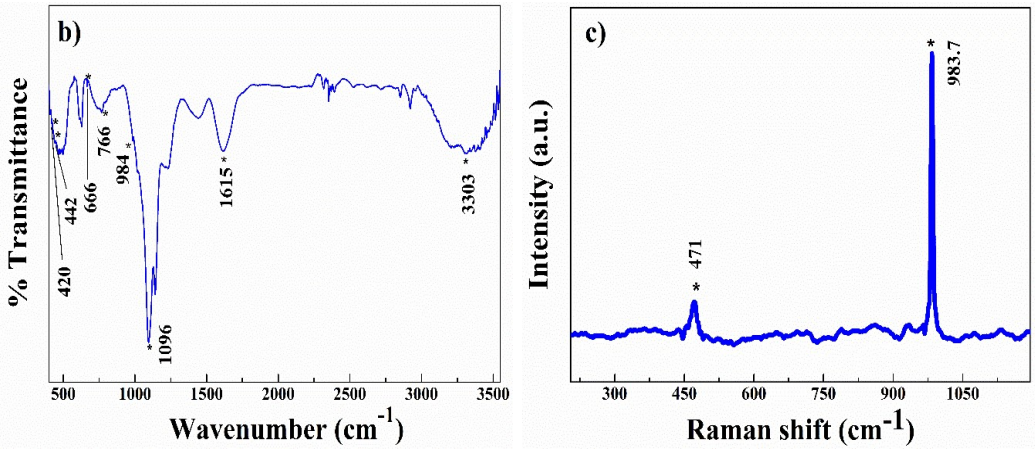

Fig. 3.2 (b) FT-IR spectra of β-NiS nanoparticles and **(c)** Raman spectra of β-NiS nanoparticles

3.3.4 Bandgap Measurement and Surface Area Analysis

Fig. 3.2d presents the UV-visible spectrum showing an absorption peak around 212 nm, confirming the formation of β-NiS nanoparticles, [4] while their particles uniformity and narrow particle size distribution is confirmed based on the narrow width of this absorption peak which is in fair agreement with the results of XRD and Raman spectra. The band gap of β-NiS nanoparticles was obtained using the Tauc plot (inset of Fig. 3.2d) and was found to be 2.08 eV. Fig. 3.2e illustrates the BET surface area measurements of the β-NiS nanoparticles. The nitrogen adsorption and desorption isotherm exhibits type IV isotherm characteristics which correlate to a complex blend of micro and mesoporous structure for β-NiS nanoparticles. The calculated BET-

specific surface area is 64 m^2/g, with average diameters of 23 nm for both micropores and mesopores. The high surface area and mesoporous nature of β-NiS nanoparticles offers better contact for the electrolyte and contribute to excellent electrochemical kinetics by increasing the charge carriers. [17] The size of mesopores for β-NiS is much bigger than the OH^- ions in an aqueous KOH electrolyte. [18]

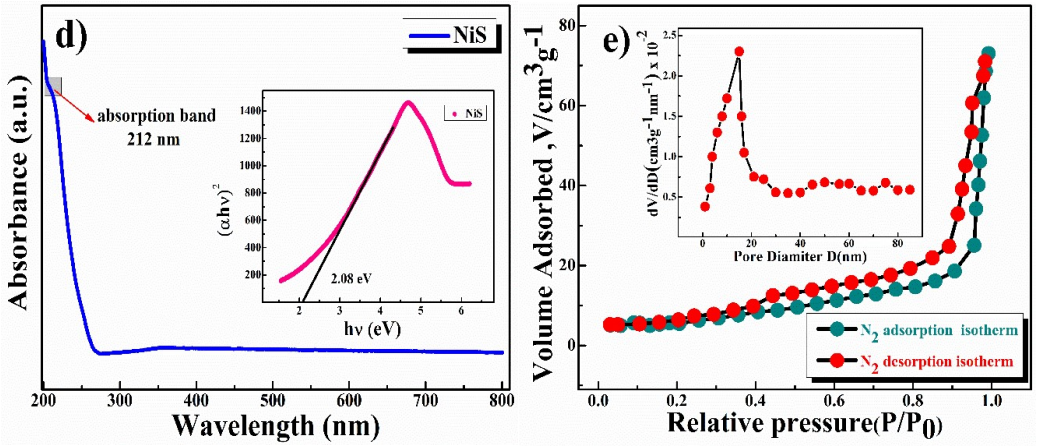

Fig. 3.2 (d) UV-Visible spectra (Tauc plot in the inset) and **(e)** BET nitrogen adsorption/desorption isotherm of β-NiS nanoparticles.

3.3.5 XPS Analysis

The electronic structure of the β-NiS sample was studied by employing X-ray photoelectron spectroscopy (XPS). The high-resolution Ni (2*p*) spectrum, in Fig. 3.3a,

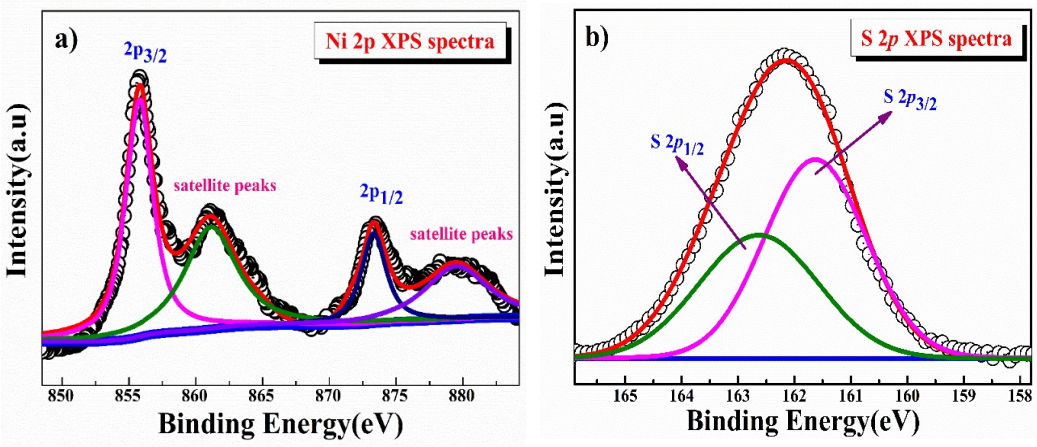

Fig. 3.3 XPS plot of β-NiS nanoparticles, (a) Ni (2*p*) spectra and (b) S (2*p*) spectra.

shows two peak at 855.8 and 873.3 eV corresponding to $2p_{3/2}$and $2p_{1/2}$ respectively of Ni^{2+} (eV) ions. The corresponding satellite peaks appears at 861.09 and 873.31 eV. The S $2p_{3/2}$ peak, in Fig. 3.3b, appears at 162.16 eV is due to S^{2-} ion. [19]

3.3.6 FE-SEM and HR-TEM Analysis

The SEM image in Fig. 3.4a displays the particle distribution and spongy-like arrangement of the β-NiS nanoparticles. The β-NiS nanoparticles are highly agglomerated, and sub-micron size grains are visible. Fig. 3.4b depicts the EDX (energy dispersive X-ray) analysis image confirming the composition of the material. HRTEM image, in Fig. 3.4c, of as-synthesized β-NiS nanoparticles shows atomic arrangements at localized regions within the sample. Fig. 3.4d shows the selected area electron diffraction (SAED) pattern shows clear well-aligned diffraction spots, indicates lattice spacing of 0.29, 0.27, 0.22, 0.18, 0.17 and 0.16 nm corresponds to (101), (300), (211), (131), (401) and (321) planes respectively. Fig. 3.4e shows the lattice fringes of β-NiS nanoparticles confirming the crystalline nature of nanoparticles. Insets (i, ii, and iii) show FFT (fast Fourier transform) image, inverse FFT, and d-spacing of β-NiS nanoparticles measured with Gatan Microscopy Suite (Digital Micrograph). The calculated d-spacing value was 0.27 nm, which matches the [300] plane of the β-NiS nanoparticles.

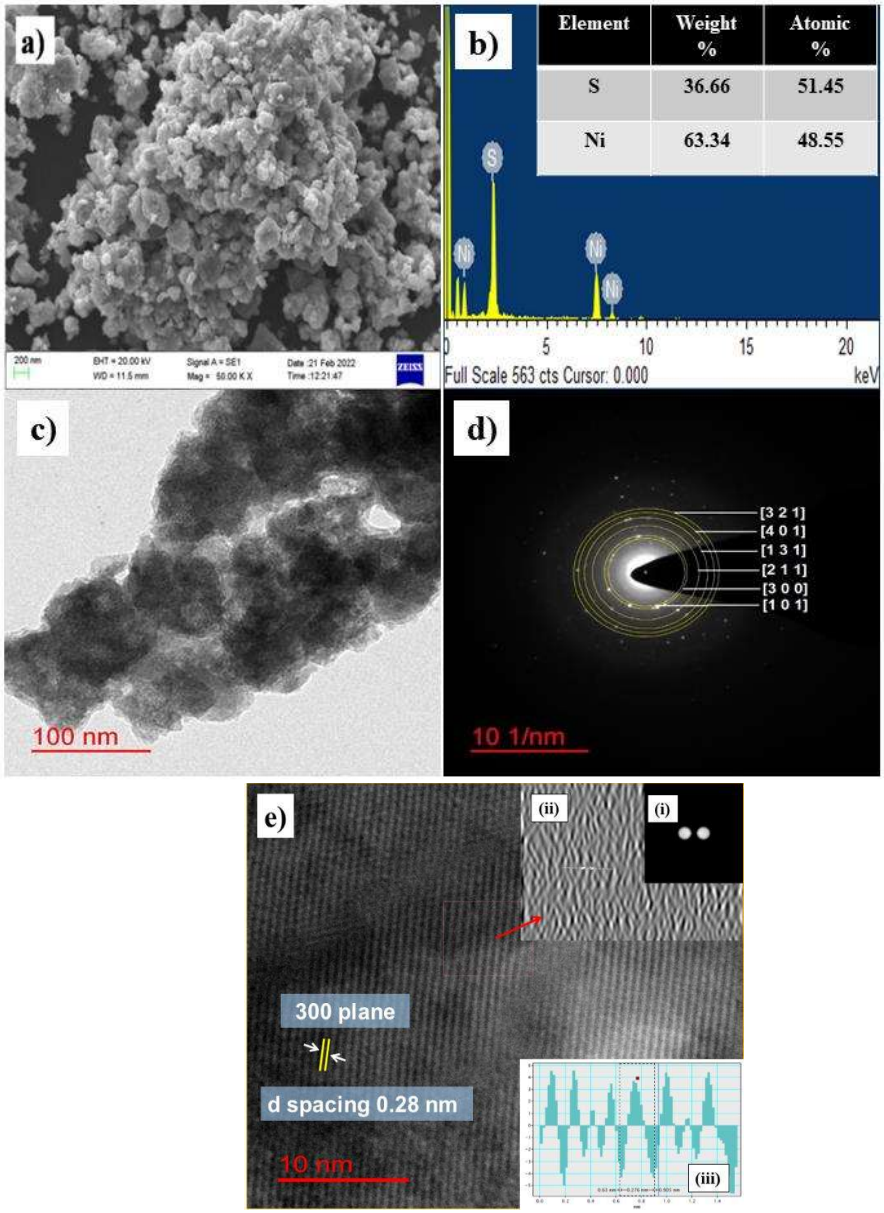

Fig. 3.4 (a) FE-SEM images, **(b)** EDX analysis image, **(c)** HRTEM, **(d)** SAED pattern shows the lattice & **(e)** Lattice fringes. Inset of (e) (i, ii, and iii) of β-NiS nanoparticles with FFT, inverse FFT picture and d-spacing.

3.3.7 Electrochemical Studies:

3.3.7.1 Cyclic Voltammetry Analysis

The charge-storage capacity of the β-NiS nanoparticles electrodes was first evaluated by using cyclic voltammetry (CV) in a three-electrode system where β-NiS nanoparticles were employed as a working electrode, platinum electrode as the counter electrode, and saturated Hg/HgO (1 M KOH) as a reference electrode in KOH electrolyte. The CV curves were measured in different concentrations of KOH, namely 0.5, 1, 2, 4, and 6 M. From the KOH concentration vs. mass-specific capacitance plot depicted in Fig. 3.5a, the mass-specific capacitance was calculated using equation 3.4; the mass-specific capacitances are 723, 806, 1611, 1094, and 864 F/g at 1 mVs^{-1} in 0.5, 1, 2, 4 and 6 M KOH respectively. The specific capacitance initially rises as the OH^- concentration increases and reaches its maximum capacitance in 2 M KOH solution and then falls as the OH^- concentration rises further. [20]

$$\boldsymbol{C} = \frac{\int_{E_1}^{E_2} \boldsymbol{i}\,(\boldsymbol{E})\boldsymbol{dE}}{\boldsymbol{2\,m\,v\,(E_2 - E_1)}} \qquad (3.4)$$

where C is the capacitance in F/g, $(E_2 - E_1)$ is the width of the potential window (V), the integral $\int_{E_1}^{E_2} i\,(E)dE$ is the total voltammetric charge obtained by the integration of both positive and negative sweeps in a CV curve. Hence, the factor of 1/2 is used to calculate charge in either the forward or backward scan, $i(E)$ is the instantaneous current (A), m is the mass (g) of active material and v is the scan rate ($V\ s^{-1}$).

The CV curve shown in Fig. 3.5c (2M KOH) depicts the presence of one pair of well-separated redox peaks at +0.37/+0.20V. The curve's nature explains the pseudocapacitive behavior coupled with surface redox (electrosorption). [21] Redox peaks originated due to the reversible transformation of Ni^{2+} toNi^{3+} through electrosorption (redox) of OH^- ions, as represented in equation 3.5. [22]

$$Ni^{2+}S^{2-} + KOH \leftrightarrow K^{+}[Ni^{3+}S^{2-}\text{-}OH^{-}] + e^{-} \quad (3.5)$$

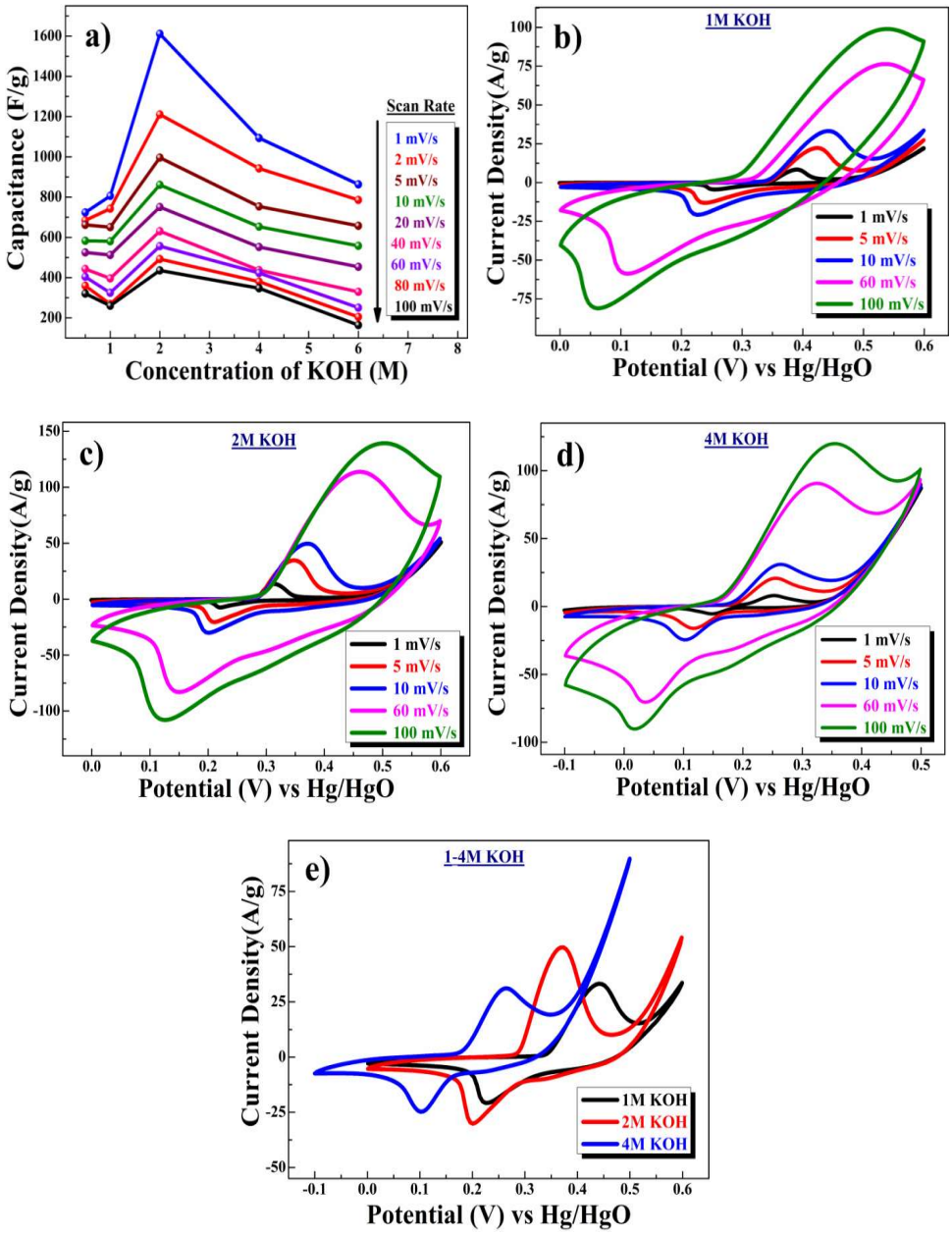

Fig. 3.5 (a) Plot of KOH concentrations vs. specific capacitance at various scan rates. Typical CV curves for β-NiS electrode in **(b)** 1 M, **(c)** 2 M and **(d)** 4 M KOH solutions at different scan rates of 1, 5, 10, 60 and 100 mVs^{-1}, and **(e)** Comparative CV study in different concentrations of electrolytes at 10 mV/s.

The CV curves at different scan rates ranging from 1 to 100 mVs^{-1} are shown in Fig. 3.5 (b, c & d). The specific capacitances from the CV curve were calculated using equation 3.4, and capacitance was found close to 1611, 1211, 996, 861, 751, 631, 556,

492 and 435 F/g at scan rates of 1, 2, 5, 10, 20, 40, 60, 80, and 100 mVs^{-1} respectively for 2M KOH. Because active areas of the electrode are more accessible for electrochemical reaction at lower scan rates, the specific capacitance drops as the scan rate increases. With higher scan rates, the anodic peak potential shifts to a more favourable position while the cathodic peak potential shifts to a more hostile position.

Fig. 3.5e shows the comparative CV study at 10 mV/s in different concentrations of electrolytes ranging from 1 to 4 M. According to the study, redox potentials are pH dependant and redox potential is shifted to a lower value with increasing concentration of electrolyte KOH, and it is not desirable for high-voltage supercapacitors applications. Further, current density values confirm that the capacitance value increase from 0.5 to 2 M KOH concentration and then it decreases above 2 M KOH concentration. [23]

3.3.7.2 Determination of Diffusion Coefficient

Fig. 3.5f shows the linear relation between cathodic and anodic peak current concerning the square root of scan rate ($\upsilon^{1/2}$), indicating that the CV curve exhibits a semi-infinite diffusion-controlled process. Furthermore, the diffusion kinetics of electrodes can be better understood by determining the diffusion coefficient. The diffusion coefficient for the electrode was determined using the Randles-Sevick equation as represented in equation 6. [24, 25]

$$i_p = 2.686 \times 10^5 \times n^{3/2} A\, D^{1/2}\, C_o\, v^{1/2} \qquad (3.6)$$

where i_p is peak current (A), n is the number of electrons transferred in the redox reaction (usually 1), A is electrode area in cm^2, D is diffusion coefficient in cm^2/s, C_o is the concentration of OH^- ion in mol/cm^3, υ is the scan rate in V/s. The diffusion coefficient (D) of hydroxide (OH^-) ions diffusion was found to be $3.13\times10^{-7} cm^2/s$ for oxidation and 0.92×10^{-7} cm^2/s for reduction, respectively for the β-NiS electrode.

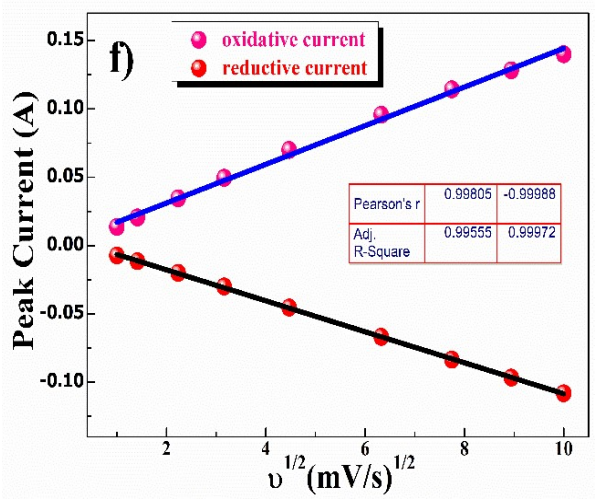

Fig. 3.5 (f) Plot of peak current vs. square root of the scan rate for diffusion kinetics of β-NiS electrode.

3.3.7.3 Kinetics Studies (Determination of *b* values) and Dunn's plot analysis

The power law provided in equation 3.7 was employed to further evaluate the qualitative contribution of the various charge storage kinetics/mechanisms of the β-NiS electrode. [26]

$$i = av^b \qquad (3.7)$$

where i is the current (A), values of a and b are adjustable, and v is the scan rate (V/s). The b value lies between 0.5−1, b = 0.5 stands for the semi-infinite diffusion control reaction for battery (intercalative behavior) type material, while b = 1 stands for the surface control capacitive reaction or electrosorption. [27]

The slopes of the corresponding log (v) versus log (i) plots, in Fig. 3.6a, for the b-values of oxidative and reductive current were found to be 0.58 and 0.58, respectively, indicating the dominance of semi-infinite diffusion-controlled intercalative processes during the electrochemical reaction resulting in battery-type supercapacitor behavior. The high specific capacitance of β-NiS nanoparticles is attributed to both semi-infinite diffusion-controlled and surface-control redox (non-diffusion) mediated

pseudocapacitance processes. Trasatti [28] and Dunn's [29] methods are adopted to evaluate the contributions of diffusion-controlled and non-diffusion-controlled capacitance concerning the experimental data.

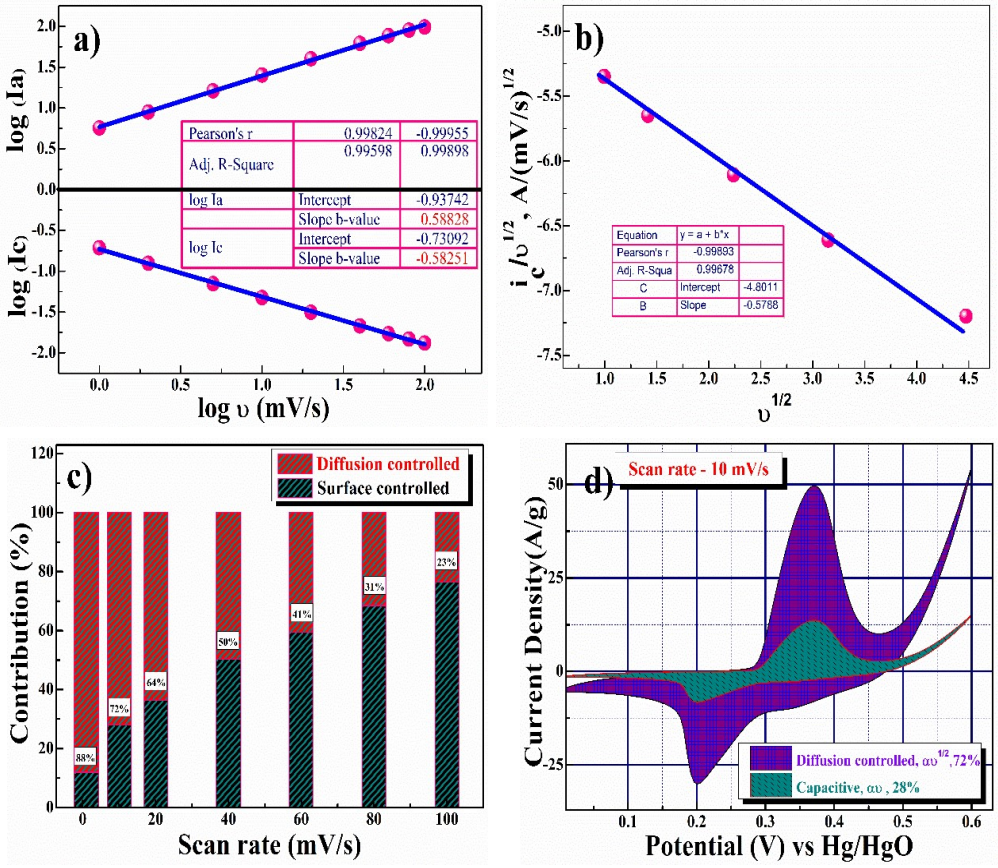

Fig. 3.6 Electrodynamic characteristics of the β-NiS electrode; **(a)** Plot of the linear relationship between log (peak current) and log (scan rate) at two different scan rate regions, **(b)** Plot of the power law of the charged state at potential and discharged state at a potential, **(c)** Diffusive and capacitive contribution at different scan rates and **(d)** Analysis of kinetic contribution at 10 mVs^{-1}.

Fig. 3.6b shows dependence of quantitative voltammetry sweep rate on the capacitive contribution to the current response. The current response at a fixed potential is the contribution of two separate mechanisms, surface capacitive effects, and diffusion-controlled insertion or intercalation.

$$i(\upsilon) = k_1\upsilon + k_2\upsilon^{1/2} \qquad (3.8)$$

For better understanding, eq. 3.8 was modified as

$$\frac{i(\upsilon)}{\upsilon^{1/2}} = \frac{k_1}{\upsilon^{1/2}} + k_2 \qquad (3.9)$$

In eq. 3.8, $k_1\upsilon$ and $k_2\upsilon^{1/2}$ represent the current contributions from the surface capacitive and diffusion-controlled intercalation processes, respectively. Thus, after the determination of k_1 and k_2, from obtaining the slope and intercept of the y-axis from linear fit, we can quantify their contribution to the current density at specific potentials. [30]

The representative curve {(V)/$\upsilon^{1/2}$ vs. $\upsilon^{1/2}$} shown in Fig. 3.6c represents the contribution of surface capacitance and diffusion-controlled intercalation at different scan rates. Fig. 3.6d represents a specific contribution at a 10 mVs^{-1} scan rate, and the contribution of surface capacitance or electrosorption was found to be 28%, and that of diffusion-controlled intercalation was found to be close to 72%.

3.3.7.4 Trassati's Plot Analysis

Trasatti plot was further used to determine the amount of charge stored in the outer and inner surfaces. According to Trassati, the electrode's inner (C_{in}) and outer surface (C_{out}) capacitance adds to the total specific capacitance (C_{Total}), and can be expressed as

$$C_{Total} = C_{in} + C_{out}(\text{F/g}) \qquad (3.10)$$

The charge storage method is reliant on the scan rate from CV analysis. Fig. 3.6e shows the linear fit of C^{-1} vs. $\upsilon^{1/2}$ at different scan rates, and the y-intercept represents the amount of total charge storage or capacitance of the electrode. Fig. 3.6f shows the linear fit C vs. $\upsilon^{-1/2}$, and the y-intercept represents the electrode's outer surface charge storage or capacitance. The C_{total}, which was determined by computing the y-intercept value used on the Trassati plot, was found to be 1751 F/g, C_{in} was found to be 1341 F/g (76.6% of the total capacitance value), and C_{out} was found to be 410 F/g (23.4% of the total

capacitance value). This confirms that 77% of the charge stored in β-NiS electrodes was due to pseudocapacitive intercalation-type behavior. Overall, it can be concluded that β-NiS nanoparticles store charge predominately through the intercalative pseudocapacitive charge storage process.

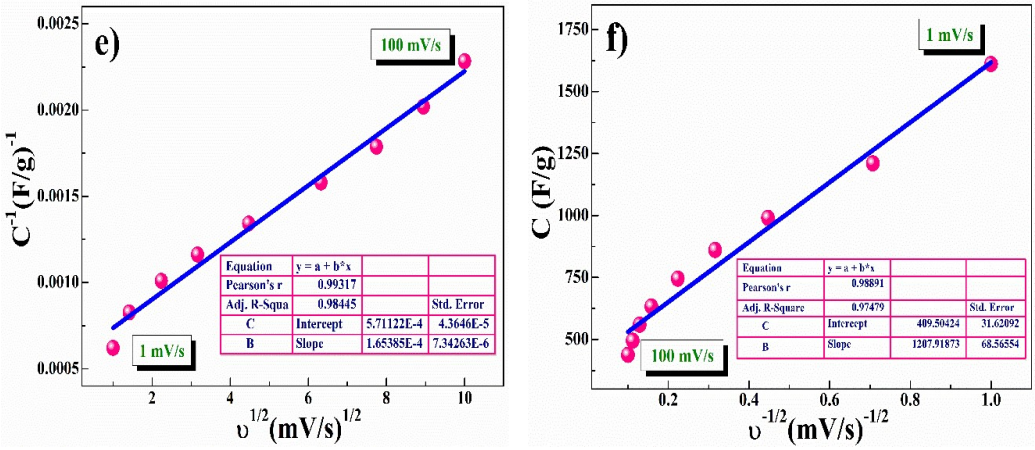

Figure 3.6 (e, f) Trasatti plot at different scan rates

3.3.7.5 Chronoamperometry Charge/Discharge Analysis

Galvanostatic charge-discharge studies were conducted for a more precise capacity assessment of β-NiS electrodes. The specific capacitance, C_{sp}, of the electrode can be calculated from the charge-discharge curve using equation 3.11. [6]

$$Csp = \frac{I\Delta t}{m\Delta V} \qquad (3.11)$$

where I is the discharge current (A), Δt is the discharge time (s), m is the mass of the active material in the electrode (g), and ΔV is the potential change during discharge (V). Fig. 3.7a depicts the specific capacitances of 1578, 1516, 1410, 1177 and 944 F/g at current densities of 1, 2, 3, 5 and 10 A/g, respectively. According to the above GCD observations, specific capacitance decreased gradually as current density increased. The specific capacitance falls to 40% of its starting value in the required current density range. Fig. 3.7b shows the capacitance value of the cycle number with a different

current density of the β-NiS electrode. Fig. 3.7c exhibits the excellent long-term cyclic stability of the β-NiS electrode at 10 A/g for 10000 cycles. 86% capacity retention reflects that the specific capacitance of the electrode did not change that much from the initial capacitance after 10000 cycles. The electrode's coulombic efficiency $\left(\eta = {}^{t_d}/_{t_c}\right)$ was 90.5% after 10000 cycles of continuous charge/discharge, which reveals the high reversibility of the β-NiS electrode. Fig. 3.7d shows the comparative study of GCD at 1 M, 2 M, and 4 M KOH concentrations.

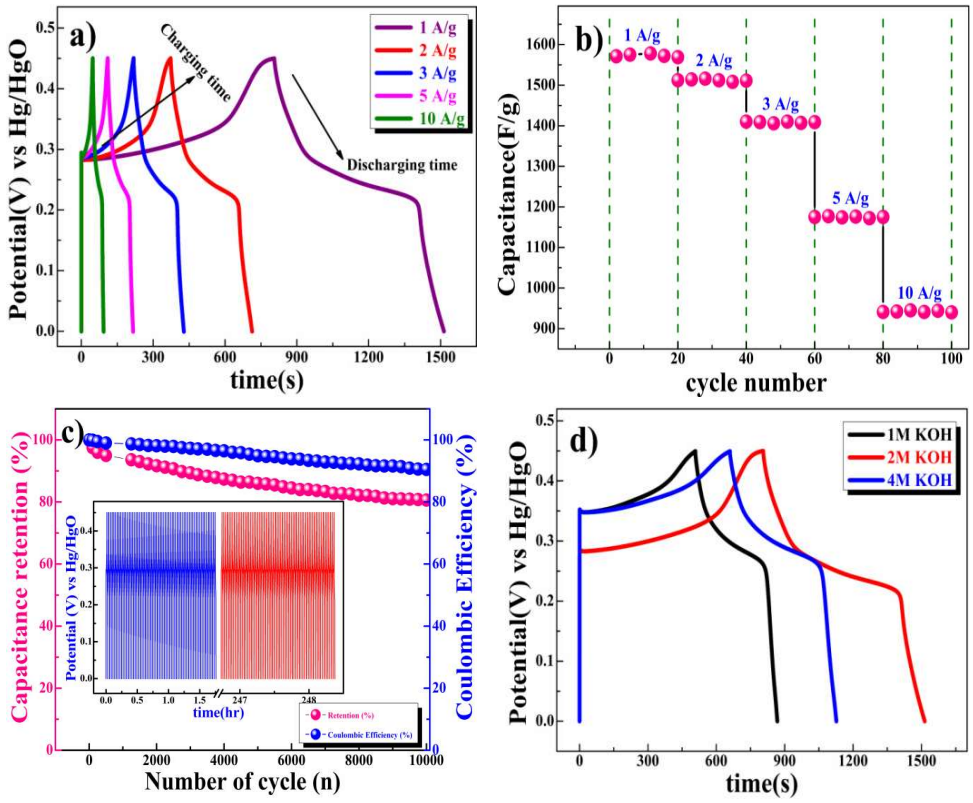

Fig. 3.7 (a) Charge/discharge curve of β-NiS electrode, **(b)** Capacitance performance of β-NiS electrode at different constant current density, **(c)** Capacitance retention and coulombic efficiency β-NiS electrode and **(d)** Comparative study of GCD at 1 M, 2 M and 4 M KOH concentration.

It is clear from the discharge time that the electrode delivers a longer discharge time in 2 M KOH electrolyte compared to 1 and 4 M KOH electrolyte at a 1 A/g current rate. The specific capacitance of the electrode was calculated from the charge-discharge

curve are 801, 1578 and 1042 F/g for 1, 2 and 4 M KOH electrolyte concentrations, respectively. According to comparative GCD observations, we confirmed an increase in specific capacitance value from 1 to 2 M KOH concentration and then a decrease in capacitance in 4 M KOH concentration which is in fair agreement with the results of the CV study.

3.3.7.6 Analysis of Electrochemical Impedance Spectroscopy (EIS)

In addition to electrochemical stability, electrochemical impedance spectroscopy (EIS) in the frequency range of 100 to 0.1 Hz at 10 mV applied potential were performed, as shown in the Nyquist plot in Fig. 3.7e. Bode plot shown in Fig. 3.7f illustrates the phase angle of the β-NiS electrode with respect to the applied frequency. The phase angle of the β-NiS electrode was 57.2° and 53.2° for the initial and after 2500 cycles, respectively. The lower phase angle (around 50°) affirms the pseudocapacitive nature of the β-NiS electrode which is in good agreement with the Nyquist plot. [31, 32]

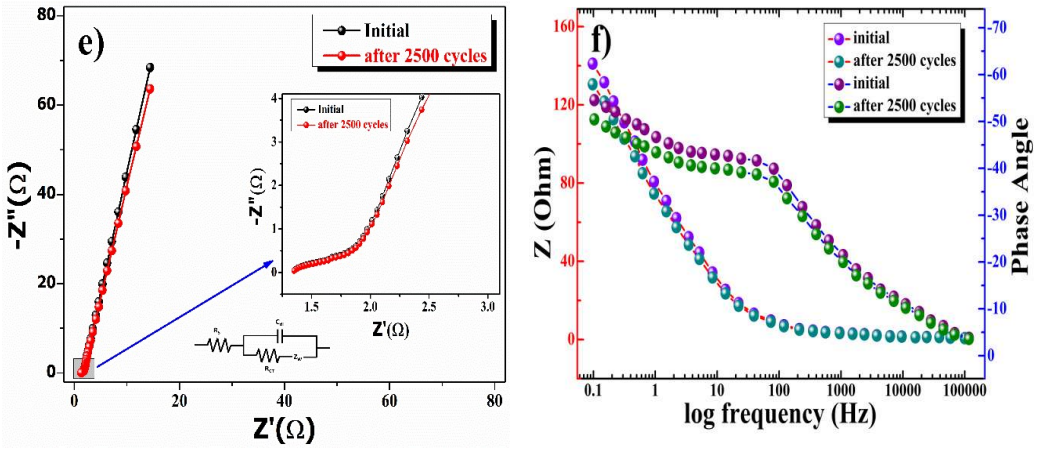

Fig. 3.7 (e) Nyquist and **(f)** Bode plot of β-NiS electrode at 10 mV between 0.1 and 100 kHz (inset displays enlarged view of Nyquist plot at high-frequency region).

The specific impedance contribution was attributed to the impedance distributions over charge transfer resistance (R_{ct}), electric series resistance (R_s) and Warburg impedance (R_w). The R_s and R_{ct} values for the β-NiS electrode were 1.34 and 0.33 Ω, respectively

(see the enlarged view in the inset of Fig. 3.7e). Lower frequency data show the Warburg diffusion resistance for the β-NiS electrode. The straight line in the low-frequency region indicates a fast OH^- ion diffusion-controlled process. EIS spectra after 2500 repeated charge-discharge cycles compared with the first cycle demonstrate the good electrochemical stability of the β-NiS electrode.

3.3.7.7 Electrochemical Charge Storage Behaviour in Neutral Na_2SO_4 Electrolyte

Further, studies were conducted to understand the charge storage behavior of β-NiS electrodes in a neutral electrolyte of 0.5 M Na_2SO_4. The CV curve at various scan rates, as shown in Fig. 3.8a, indicates well-separated redox peaks (+0.68/+0.48 V at 1 mVs^{-1} scan rate). Specific capacitance, which is the function of scan rate, has been estimated with 0.5 M Na_2SO_4 electrolyte are 403, 323, 238, 117 and 79 F/g at 1, 5, 10, 60 and 100 mVs^{-1} respectively was obtained. Fig. 3.8b displays the findings of the quantitative galvanostatic charge/discharge storage measurement and the results were found to be 386, 308, 195, 115 and 71 F/g at 1, 2, 3, 5 and 10 A/g respectively. Subsequently, a comparative study was carried out to study the effects of anions present in the electrolyte. Fig. 3.8c shows the comparative CV curve of the β-NiS electrode in 0.5 M Na_2SO_4 and 2 M KOH electrolytes. There were changes in the redox peaks from KOH to Na_2SO_4 electrolyte. Further, in comparison to 0.5 M Na_2SO_4, the redox peaks were found to be more dominant in 2 M KOH; this may be due to the size difference of hydration radii of hydroxyl ions (3 Å) as compared to sulfate ions (3.79 Å). A larger SO_4^{2-} hydrate sphere further reduces the number of ions that enter the pores, which results in slower diffusion and reduced production of electric double layers. [33] Additionally, the greater molar conductance of the OH^- ion (198 $cm^2\ \Omega\ mol^{-1}$) in the KOH electrolyte compared to SO_4^{2-} (79.8 $cm^2\ \Omega\ mol^{-1}$) in Na_2SO_4 exhibits a more robust current response in the CV curve. [33]

GCD experiments were carried out in 2 M KOH and 0.5 M Na_2SO_4 electrolytes to determine the electrode's quantitative capacitance. It is clear from Fig. 3.8d (see the discharge time) that the electrode delivers a longer discharge time in 2 M KOH electrolyte as compared to 0.5 M Na_2SO_4 electrolyte at a 1 A/g current rate. These studies corroborate the applicability of an aqueous 2 M KOH electrolyte for high electrode performance because the smaller OH^- anions match the electrode's pore width well, resulting in improved performance.

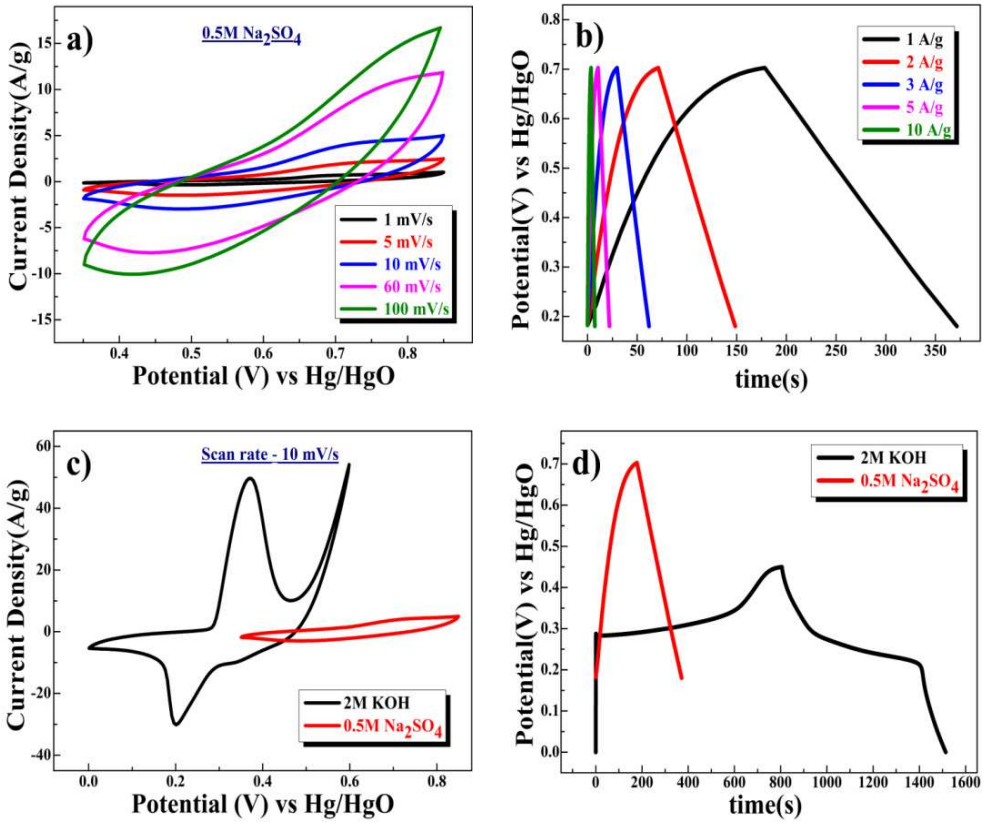

Fig. 3.8 (a) CV and **(b)** GCD plot of β-NiS electrode in 0.5 M Na_2SO_4 electrolyte, **(c)** Comparative CV diagram of β-NiS electrode in 2 M KOH and 0.5 M Na_2SO_4 electrolyte at 10 mV/s and **(d)** Comparative charge/discharge curve of β-NiS electrode in KOH and Na_2SO_4 medium at 1A/g.

3.3.7.8 Asymmetric full cell test of β-NiS//AC (CV, GCD, and Cyclic Stability)

Two electrode measurements have been conducted in 2 M KOH to understand the usable charge storage behavior of the β-NiS electrode using AC as a counter electrode. To evaluate the maximum specific capacitance (C_{total}) during the full cell test, the storage capacity of positive ($C_{positive}$) and negative electrodes ($C_{negative}$) must be balanced using equation 3.12.

$$\frac{1}{C_{total}} = \frac{1}{C_{positive}} + \frac{1}{C_{negative}} \qquad (3.12)$$

Equation 3.13 was used to calculate the mass ratio (m^+/m^-) of the positive and negative electrode material to balance the charge storage capacity of the cell.

$$\frac{m^+}{m^-} = \frac{C_- \times \Delta E_-}{C_+ \times \Delta E_+} \qquad (3.13)$$

$m^+, m^-, C_+, C_-, \Delta E_+, \Delta E_-$ are mass, specific capacitance, and potential window of positive and negative electrodes estimated by three-electrode measurements. [34]

Fig. 3.9a shows CV curves at a 10 mV/s scan rate where the β-NiS electrode was used as the positive electrode and AC was used as the negative electrode. As AC is used to increase the conductivity of the active electrode, therefore, while calculating the electrochemical charge storage capacity of the NiS electrode, the contribution in capacitance due to AC is extracted and the obtained data shows the capacitive value of the NiS electrode only. The calculated mass ratio (m^+/m^-) was 1: 1.67 for the asymmetric cell and the weight of the active material was measured to be 4.45 mg (excluding the weight of acetylene black and PVDF). Fig. 3.9b shows the CV plot of β-NiS electrode//AC, a two-electrode ASCs (asymmetry supercapacitor cell at scan rates ranging from 1−100 mVs^{-1} in the potential window 0-1.5 V. Fig. 3.9c shows the GCD curve and the specific capacitance values were calculated using equation 3.11. Capacitance values were 780, 716, 622, 494 and 326 F/g at current densities of 1, 2, 3,

5, and 10 A/g, respectively. β-NiS//AC (ASC) full cell shows brilliant long-term cyclic stability with 90% capacity retention after 2500 cycles, as shown in Fig. 3.9d. Coulombic efficiency of two-electrode cells has lost only 4% of its initial value after 2500 cycles.

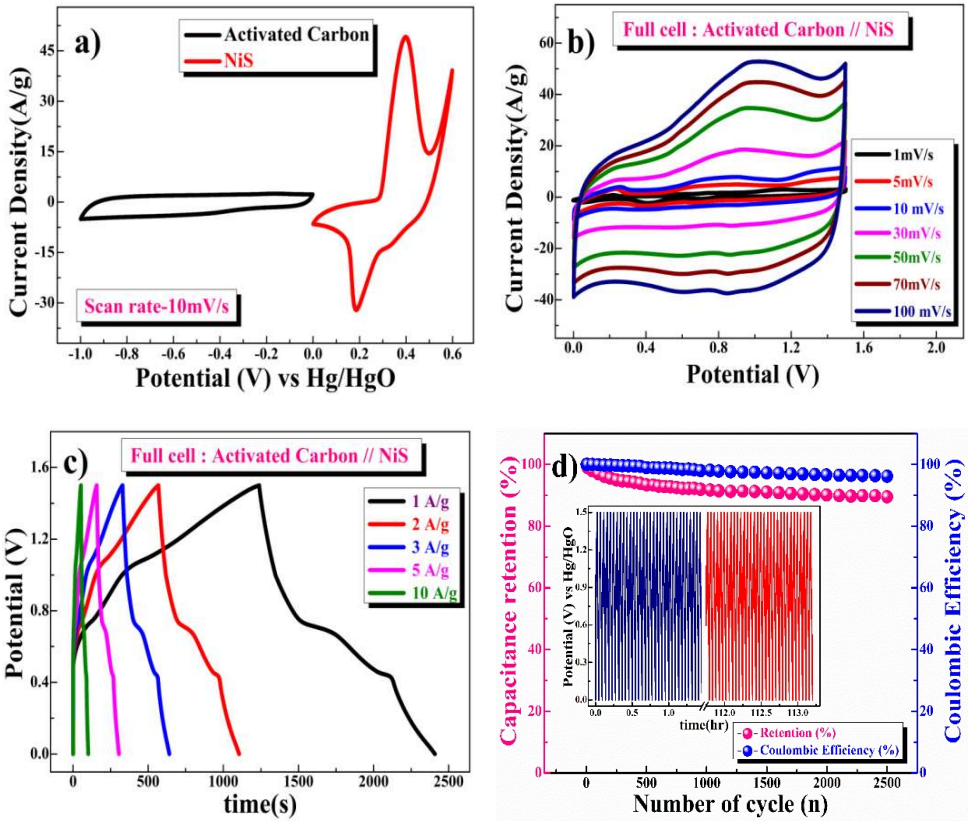

Fig. 3.9 (a) Separate CV plots for activated carbon and β-NiS electrode in 2 M KOH electrolyte at 10 mV/s, **(b)** CV at different scan rates, (c) Charge-discharge at different current rates and (d) Capacitance retention and coulombic efficiency.

3.3.7.9 Electrochemical Impedance Spectroscopy (EIS) of β-NiS//AC Full Cell

Fig. 3.9e & 3.9f illustrates the EIS (Nyquist and Bode) plots in the frequency range of 0.1 -100 kHz at 10 mVs^{-1} applied potential confirming the retention of the electronic structure. The resistance of the full cell (β-NiS electrode//AC) decreases after completion of 2500 cycles compared to the first cycle. From Fig. 3.9f, it is evident that the phase angle at the tail is 54.6° & 51.6° for the initial and after 2500 cycles, respectively which further confirms the pseudocapacitive nature of the β-NiS//AC cell.

The EIS result corroborates the cyclic stability by demonstrating a little difference in the cell's internal and charge transfer resistance before and after the test.

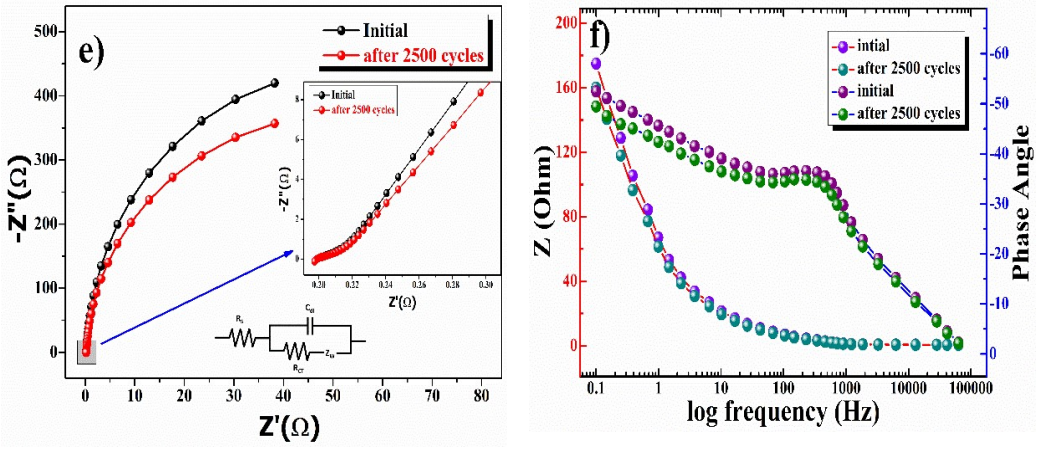

Fig. 3.9 (e) Nyquist and **(f)** Bode plot at 10 mV at initial cycle and after 2500 cycle of full cell formation.

3.3.7.10 Study of Energy Density vs Power Density of β-NiS//AC Full Cell

Power and energy density of asymmetric cell capacitors were calculated using equation 3.14 & 3.15.

$$P(W/kg) = \frac{E \text{ X } 3600}{t_{dis}} \qquad (3.14)$$

$$E(Wh/kg) = \frac{1}{2}\frac{C_{ASC}}{3.6}\Delta V^2 \qquad (3.15)$$

where C_{sp} is specific capacitance, V is operating voltage, and t_{dis} is discharge time.

Fig. 3.9g displays the Ragone plot (specific energy vs. specific power) of β-NiS electrode//AC (ASC) full-cell device in comparison with reported supercapacitor devices. Resultant values of asymmetric cells confirm the highest specific energy equivalent to ~163 Wh/kg at 1 A/g current density and specific power equivalent to ~507 W/kg. Maximum specific power of ~5021 W/kg was obtained when specific energy was reduced to ~ 68 Wh/kg at 10 A/g of current density.

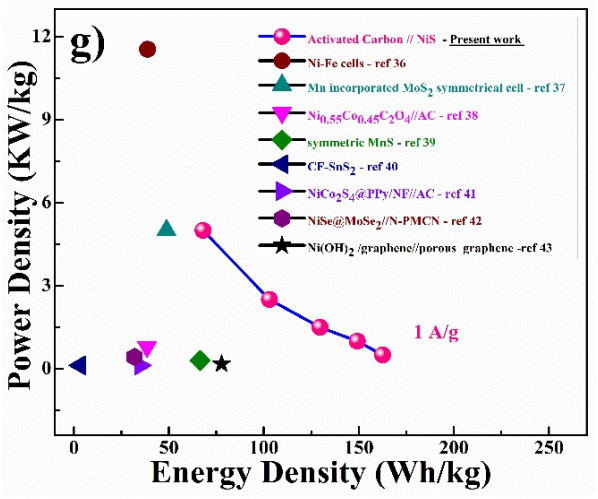

Fig. 3.9 (g) Ragone plot of the β-NiS//AC fuel cell in ASC mode in comparison with reported supercapacitor devices.

The obtained energy and power density values of β-NiS electrode//AC (ASC) incorporated MoS_2, $Ni_{0.55}Co_{0.45}C_2O_4$//AC, SnS_2 and others as electrode materials shown in Table 3.2. [35]

Table. 3.2 Displays the Ragone plot of β-NiS electrode//AC (ASC) device in comparison with reported supercapacitor devices.

Material	**Energy density** (Wh/kg)	**Power density** (KW/kg)	**Ref.**
Ni − Fe Cells	38.78	11.54	[36]
Mn incorporated MoS_2	48.8	5	[37]
$(Ni_{0.33}Co_{0.67})Se_2$ complex	29.1	0.8	[38]
MnS thin films	66.41	0.3	[39]
$NiCo_2S_4$ nanoplate	35	0.12	[40]
CF-SnS_2	3.1	0.123	[41]
NiSe@$MoSe_2$//N-PMCN	32	0.425	[42]
$Ni(OH)_2$/graphene//graphene	77.8	0.174	[43]
β-NiS nanoparticles	**68** **103** **129.6** **149.2** **162.5**	**5** **2.51** **1.5** **1** **0.5**	**Present work**

3.4 Conclusions

In summary, β-NiS nanoparticles were synthesized using a simple precipitation route where H_2S generated through the Kipp generator method was used as a precipitating agent for sulfide formation in an aqueous medium. High diffusion of gas into the liquid phase resulted in the formation of single-phase β-NiS nanoparticles. The XRD pattern shows that the formation of more stable β-NiS nanoparticles is in the rhombohedral millerite phase, and the grain size estimated using the Debye Scherrer equation was approximately 10 nm. Nanocrystalline β-NiS shows the quantum confinement effect due to the smaller/nanocrystalline size of the particles by Raman spectra and supported by XRD and UV-Visible spectroscopy data. Nanocrystallineβ-NiS electrode showed highly pseudocapacitive performance with a specific capacitance of 1611 F/g at $1mVs^{-1}$ in a potential window of 0-0.6 V in CV and 1578 F/g at a current density of 1 A/g in the potential window of 0-0.45 V in GCD measurement. Further, excellent cyclic stability and predominant intercalative mechanism seem to operate behind the high charge storage capacity of the materials as intercalative (inner) and surface (outer) charges stored by β-NiS electrodes were found to be 72% and 28%, respectively. In 2M KOH electrolyte, β-NiS//AC fuel cell resulted in ~163 Wh/kg of maximum specific energy with specific power equivalent to ~507 W/kg in the voltage window of 1.5 V in 2M KOH electrolyte at 1 A/g current density. The capacitances of different transition-metal-sulfides-based pseudocapacitors are summarized in Table 3.3, and results show that charge storage behavior and the capacitance value are comparable or superior to most of the transition-metal-sulfide-based pseudocapacitors reported to date. These findings demonstrate the potential of nanocrystalline β-NiS to serve as a pseudocapacitive electrode for large-scale energy storage applications.

Table. 3.3 Values of specific capacitance of some transition-metal sulfides.

Material	**Capacitance ($F\ g^{-1}$)**	**Current Density/ Scan Rate**	**Electrolyte**	**Ref.**
FeS_2 nanobelts	308	5 mVs^{-1}	1 M Na_2SO_4	[44]
Mn-MoS_2	430	5 mVs^{-1}	0.5 M Na_2SO_4	[37]
$(Ni_{0.33}Co_{0.67})Se_2$	828	1 A/g	3 M KOH	[38]
MnS thin films	747	1 mA cm^{-2}	1 M KOH	[39]
NiS nanorods	788	1 mA cm^{-2}	1 M KOH	[6]
$NiCo_2S_4$ nanoplate	437	1 A/g	3 M KOH	[40]
flower-like SnS_2	524	0.08 A/g	1 M KCl	[41]
CoS-AC composite	798	10 A/g	$K_3Fe(CN)_6$-KOH	[45]
β-NiS nanoparticles	**1611** **1578**	**1 mVs^{-1}** **1 A/g**	**2 M KOH**	**Present work**

3.5 References

1. Hou, L., et al., *Electrochemically induced transformation of NiS nanoparticles into Ni (OH) 2 in KOH aqueous solution toward electrochemical capacitors.* Electrochimica acta, 2011. **56**(22): p. 7454-7459.
2. Zhu, T., et al., *Hierarchical nickel sulfide hollow spheres for high performance supercapacitors.* RSC advances, 2011. **1**(3): p. 397-400.
3. Yang, J., et al., *Electrochemical performances investigation of NiS/rGO composite as electrode material for supercapacitors.* Nano Energy, 2014. **5**: p. 74-81.
4. Fazli, Y., et al., *Synthesis, characterization and photocatalytic property of nickel sulfide nanoparticles.* Journal of Materials Science: Materials in Electronics, 2016. **27**: p. 7192-7199.
5. Lei, X., et al., *Electrochemical performances investigation of new carbon-coated nickel sulfides as electrode material for supercapacitors.* Materials, 2019. **12**(21): p. 3509.
6. Gaikar, P., et al., *Synthesis of nickel sulfide as a promising electrode material for pseudocapacitor application.* RSC advances, 2016. **6**(113): p. 112589-112593.
7. Wang, H., et al., *Novel dealloying-fabricated NiS/NiO nanoparticles with superior cycling stability for supercapacitors.* ACS omega, 2021. **6**(28): p. 17999-18007.
8. Peng, L., et al., *Nickel sulfide nanoparticles synthesized by microwave-assisted method as promising supercapacitor electrodes: an experimental and computational study.* Electrochimica Acta, 2015. **182**: p. 361-367.

9. Li, Y., et al., *New design of oriented NiS nanoflower arrays as platinum-free counter electrode for high-efficient dye-sensitized solar cells.* Superlattices and Microstructures, 2019. **125**: p. 66-71.

10. Sowa, H., H. Ahsbahs, and W. Schmitz, *X-ray diffraction studies of millerite NiS under non-ambient conditions.* Physics and Chemistry of Minerals, 2004. **31**: p. 321-327.

11. Guillaume, F., et al., *Optical phonons in millerite (NiS) from single-crystal polarized Raman spectroscopy.* Journal of Raman Spectroscopy: An International Journal for Original Work in all Aspects of Raman Spectroscopy, Including Higher Order Processes, and also Brillouin and Rayleigh Scattering, 2008. **39**(10): p. 1419-1422.

12. Guo, H., et al., *Efficient adsorption and photocatalytic degradation of Congo red onto hydrothermally synthesized NiS nanoparticles.* Journal of nanoparticle research, 2013. **15**: p. 1-12.

13. Vakylabad, A.B., et al., *A procedure for processing of pregnant leach solution (PLS) produced from a chalcopyrite-ore bio-heap: CuO Nano-powder fabrication.* Hydrometallurgy, 2016. **163**: p. 24-32.

14. Kristl, M., et al., *Synthesis of nickel and cobalt sulfide nanoparticles using a low cost sonochemical method.* Heliyon, 2017. **3**(3).

15. Muhamed Shajudheen, V., et al., *Structural and optical properties of NiS nanoparticles synthesized by chemical precipitation method.* IJIRSET, 2016. **5**: p. 15099-15103.

16. Indhumathy, M. and A. Prakasam, *Controllable synthesis of NiS/rGO hybrid composite: an excellent counter electrode for dye sensitized solar cell.* Journal of Cluster Science, 2020. **31**(1): p. 91-98.

17. Behnoudnia, F. and H. Dehghani, *Anion effect on the control of morphology for NiC 2 O 4· 2H 2 O nanostructures as precursors for synthesis of Ni (OH) 2 and NiO nanostructures and their application for removing heavy metal ions of cadmium (II) and lead (II).* Dalton Transactions, 2014. **43**(9): p. 3471-3478.

18. An, L., et al., *Highly ordered mesoporous NiCo 2 O 4 with superior pseudocapacitance performance for supercapacitors.* Journal of Materials Chemistry A, 2015. **3**(21): p. 11503-11510.

19. Shombe, G.B., et al., *Direct solvent free synthesis of bare α-NiS, β-NiS and α-β-NiS composite as excellent electrocatalysts: Effect of self-capping on supercapacitance and overall water splitting activity.* Scientific reports, 2020. **10**(1): p. 3260.

20. Gupta, A., et al., *SrFeO 3− δ: a novel Fe 4+↔ Fe 2+ redox mediated pseudocapacitive electrode in aqueous electrolyte.* Physical Chemistry Chemical Physics, 2022. **24**(18): p. 11066-11078.

21. Evanko, B., et al., *Redox-enhanced electrochemical capacitors: status, opportunity, and best practices for performance evaluation.* ACS Energy Letters, 2017. **2**(11): p. 2581-2590.

22. Nachimuthu, S., et al., *Electrochemical and magnetic properties of 3D porous NiS/CuS nanocomposites.* Applied Surface Science Advances, 2022. **7**: p. 100209.

23. Mishra, N.K., et al., *NiC2O4· 2H2O Nanoflakes: A Novel Redox-mediated Intercalative Pseudocapacitive Electrode for Supercapacitor Applications in Aqueous KOH and Neutral Na2SO4 electrolytes.* ChemistrySelect, 2022. **7**(21): p. e202201134.

24. Ramkumar, B., et al., *Synthesis and characterization of carbon coated LiCo1/3Ni1/3Mn1/3O2 and bio-mass derived graphene like porous carbon electrodes for aqueous Li-ion hybrid supercapacitor.* Journal of Physics and Chemistry of Solids, 2018. **112**: p. 270-279.

25. Mayedwa, N., et al., *Green synthesis of zin tin oxide (ZnSnO3) nanoparticles using Aspalathus Linearis natural extracts: Structural, morphological, optical and electrochemistry study.* Applied Surface Science, 2018. **446**: p. 250-257.

26. Su, D., et al., *High-capacity aqueous potassium-ion batteries for large-scale energy storage.* Advanced Materials, 2017. **29**(1): p. 1604007.

27. Fleischmann, S., et al., *Pseudocapacitance: from fundamental understanding to high power energy storage materials.* Chemical Reviews, 2020. **120**(14): p. 6738-6782.

28. Ardizzone, S., G. Fregonara, and S. Trasatti, *"Inner" and "outer" active surface of RuO2 electrodes.* Electrochimica Acta, 1990. **35**(1): p. 263-267.

29. Wang, J., et al., *Pseudocapacitive contributions to electrochemical energy storage in TiO2 (anatase) nanoparticles.* The Journal of Physical Chemistry C, 2007. **111**(40): p. 14925-14931.

30. Kim, H.-S., et al., *Oxygen vacancies enhance pseudocapacitive charge storage properties of MoO3− x.* Nature materials, 2017. **16**(4): p. 454-460.

31. Mohanadas, D., et al., *Facile synthesis of PEDOT-rGO/HKUST-1 for high performance symmetrical supercapacitor device.* Scientific reports, 2021. **11**(1): p. 11747.

32. Krishnamoorthy, K., et al., *One pot hydrothermal growth of hierarchical nanostructured Ni3S2 on Ni foam for supercapacitor application.* Chemical Engineering Journal, 2014. **251**: p. 116-122.

33. Pal, B., et al., *Electrolyte selection for supercapacitive devices: a critical review.* Nanoscale Advances, 2019. **1**(10): p. 3807-3835.

34. Subramani, K., et al., *All-solid-state asymmetric supercapacitors based on cobalt hexacyanoferrate-derived CoS and activated carbon.* RSC advances, 2017. **7**(11): p. 6648-6659.

35. Manoharan, S., et al., *Proton conducting solid electrolyte-piezoelectric PVDF hybrids: novel bifunctional separator for self-charging supercapacitor power cell.* Nano Energy, 2021. **83**: p. 105753.

36. Yao, J., et al., *Configuring optimal FeS2@ carbon nanoreactor anodes: Toward insights into pyrite phase change/failure mechanism in rechargeable Ni–Fe cells.* ACS applied materials & interfaces, 2019. **11**(45): p. 42032-42041.

37. Singha, S.S., et al., *Mn incorporated MoS2 nanoflowers: A high performance electrode material for symmetric supercapacitor.* Electrochimica Acta, 2020. **338**: p. 135815.

38. Quan, L., et al., *Construction of hierarchical nickel cobalt selenide complex hollow spheres for pseudocapacitors with enhanced performance.* Electrochimica Acta, 2018. **281**: p. 109-116.

39. Pujari, R., et al., *Synthesis of MnS microfibers for high performance flexible supercapacitors.* Materials & Design, 2016. **108**: p. 510-517.

40. Pu, J., et al., *Preparation and electrochemical characterization of hollow hexagonal NiCo2S4 nanoplates as pseudocapacitor materials.* ACS Sustainable Chemistry & Engineering, 2014. **2**(4): p. 809-815.

41. Mishra, R.K., et al., *One-step solvothermal synthesis of carnation flower-like SnS2 as superior electrodes for supercapacitor applications.* Applied Surface Science, 2017. **425**: p. 923-931.

42. Peng, H., et al., *High-performance asymmetric supercapacitor designed with a novel NiSe@ MoSe2 nanosheet array and nitrogen-doped carbon nanosheet.* ACS Sustainable Chemistry & Engineering, 2017. **5**(7): p. 5951-5963.

43. Liu, Y., et al., *Preparation of Ni (OH) 2-graphene sheet-carbon nanotube composite as electrode material for supercapacitors.* Journal of alloys and compounds, 2015. **618**: p. 37-43.

44. Chen, J., et al., *Pyrite FeS2 nanobelts as high-performance anode material for aqueous pseudocapacitor.* Electrochimica Acta, 2016. **222**: p. 172-176.

45. Xu, T., et al., *One-pot synthesis of a CoS-AC electrode in a redox electrolyte for high-performance supercapacitors.* Journal of Applied Electrochemistry, 2019. **49**: p. 1069-1077.